Morphology Engineering: A Route to Highly Reproducible and High Efficiency Perovskite Solar Cells

Dongqin Bi,[1] Jingshan Luo,[1] Fei Zhang,[1] Arnaud Magrez,[3] Evangelia Nefeli Athanasopoulou,[4] Anders Hagfeldt[2], Michael Grätzel[1]**

[1]Laboratory of Photonics and Interfaces, Ecole Polytechnique Fédérale de Lausanne, Lausanne, Switzerland

[2]Laboratory of Photomolecular Science, Ecole Polytechnique Fédérale de Lausanne, Lausanne, Switzerland

[3]Institute of Condensed Matter Physics, Ecole Polytechnique Fédérale de Lausanne, Lausanne, Switzerland

[4]Institute of Materials, Ecole Polytechnique Fédérale de Lausanne, Lausanne, Switzerland

Corresponding author: dongqin.bi@epfl.ch and michael.graetzel@epfl.ch.

Abstract

Despite the rapid increase in the performance of perovskite solar cells, they still suffer from low lab-to-lab or people-to-people reproducibility. Aiming for a universal condition to high performance devices, we investigated the morphology evolution of the composite perovskite by tuning annealing temperature and precursor concentration of the perovskite film. Here we introduce thermal annealing as a powerful tool to generate a well controlled excess of PbI_2 in the perovskite formulation and show that this benefits the photovoltaic performance. We demonstrated the correlation between the film microstructure and electronic property and device performance. An optimized average grain size/thickness aspect ratio of the perovskite crystallite is identified, which brings about a highly

reproducible power conversion efficiency (PCE) of 19.5%, with a certified value of 19.08%. Negligible hysteresis and outstanding morphology stability are observed with these devices. These findings lay the foundation for further boosting the PCE of PSC and can be very instructive in fabrication high quality perovskite films for a variety of applications, such as light-emitting diodes, field-effect transistors and photo-detectors, etc.

Key words: perovskite solar cell morphology

Introduction

Significant progress has been made on the device performance of metal halide perovskite solar cells (PSCs) during the past two years with an incessant increase of record efficiency.[1] One representative case is a photovoltaic with an ammonium derivative as A cation and lead iodide (ANH_3PbI_3, A = CH_3- or NH=CH-) as light absorbers, which form the central focus for development of low-cost and highly efficient solid-state thin film solar cells.[2] Due to the simplicity of the perovskite material itself, tremendous efforts have been devoted to the optimization of composition,[3–6] interface[7–11] and device structures[12–15]. However, reproducibility fabrication of high efficiency and stable devices has set out the ultimate challenges, because they require painstaking optimization of perovskite layers with long-term stability and careful adjustment of interfaces between different layers to reduce electron–hole recombinations. To date, a number of optimizing methods have been reported, however many of them suffer from low lab-to-lab or person-to-person reproducibility.

Among the different formulations that have been investigated, combining a composite (mixed cation and/or anion) perovskite absorber with the anti-solvent treatment procedure has so far been the most successful method of device engineering since the first report by Pellet et al.[3] and Jeon et al.[4] The perovskite films made by these techniques hold many of the merits of a good solar absorber and

converter, including high absorption coefficient, broad absorption range for high current density, efficient charge separation to ensure high open circuit voltage and at the same time negligible hysteresis. During efforts to search for a highly repeatable fabrication condition, researchers have long noticed that the annealing temperature[16] and concentration[17,18] are critical parameters that dominate the structure of perovskite absorber and the performances of final devices. Unfortunately, however, due to the complexity of the composite perovskite system, a systematic study on the optimization of this multicomponent system towards its best performing condition has not appeared so far.

Recently, by judiciously manipulating a composite perovskite absorber with non-stoichiometric composition of the precursors, we realized a perovskite solar cell with good power-conversion efficiency (PCE) of 20.8% and intense electroluminescence yield (0.5 %) with a cell configuration of FTO/TiO/perovskite/SpiroOMeTAD/Au (FTO: fluorine-doped tin oxide).[19] Besides the optimized composition ($R_{PbI2/FAI}$ = 1:05; $R_{PbI2/PbBr}$ = 5.67) in the precursor solutions, in pursuit of such high PCE and seeking for a universal condition to high performance devices, we have in the present work also investigated the morphology evolution of the corresponding composite perovskite by tuning precursor concentration and annealing temperature of the perovskite film. We demonstrate the correlation between the film microstructure and electronic property and device performance. An optimized average grain size/thickness aspect ratio of the perovskite crystallite is identified, which brings about a highly reproducible PCE of 19.5%, with a certified maximum value of 19.08%. A key innovation presented in this work is to exploit the release of methylammonium iodide from the perovskite under thermal annealing to produce a stoichiometric excess of PbI_2 which favorable affects device performance. Outstanding morphological stability is also observed with these

devices. These findings lay a foundation for further boosting the PCE of PSC and can be very instructive in fabrication high quality perovskite films for a variety of applications, such as light-emitting diodes, field-effect transistors and photo-detectors, etc.

Results and Discussion

According to Jeon et al.[4] replacing 15 mol% of FAI in $FAPbI_3$ by MABr in the presence of remnant PbI_2 leads to a stabilized trigonal perovskite phase (P3m1) and high quality perovskite film.[19] In our previous study, we introduced a stoichiometric excess of PbI_2 in our recipe and reported on a subtle correlation between the PbI_2 content of the mixed perovskite and the open circuit voltage (V_{OC}). On the other hand it is known that the excess of PbI_2 phase can be generated intentionally by controlled thermal annealing of a stoichiometric film.[20] However, uncontrolled growth of the excess PbI_2 phase will deteriorate the fill factor (*FF*) and short circuit current (J_{SC}). Aiming to find the optimal annealing conditions to obtain the best PCE, we annealed the as spin-casted film from a stoichiometric recipe of the aforementioned composition ($(FAPbI_3)_{0.85}(MAPbBr_3)_{0.15}$) with a concentration of 1.52 M in DMSO/DMF at different temperature ranging between 80°C and 180°C for 120 min. Figure 1a illustrates the temperature dependent grain growth behavior as studied by scanning electron microscopy (SEM). Statistics of grain size derived from the corresponding SEM images are shown in Fig. S1. It is known that the growth rate of a grain is determined by the difference in Gibbs free energy (ΔG_f) of the precursor and formed perovskite, including internal and surface/interface energy of the grains.[21,22] This diffusion- controlled process will speed up with the annealing temperature which will also increase the rate of desolvation. Therefore, we witnessed marked increase in mean grain size from 202 nm to 411 nm (Fig. 1a,c and S1) as the substrate temperature increases from 80°C to 180°C.

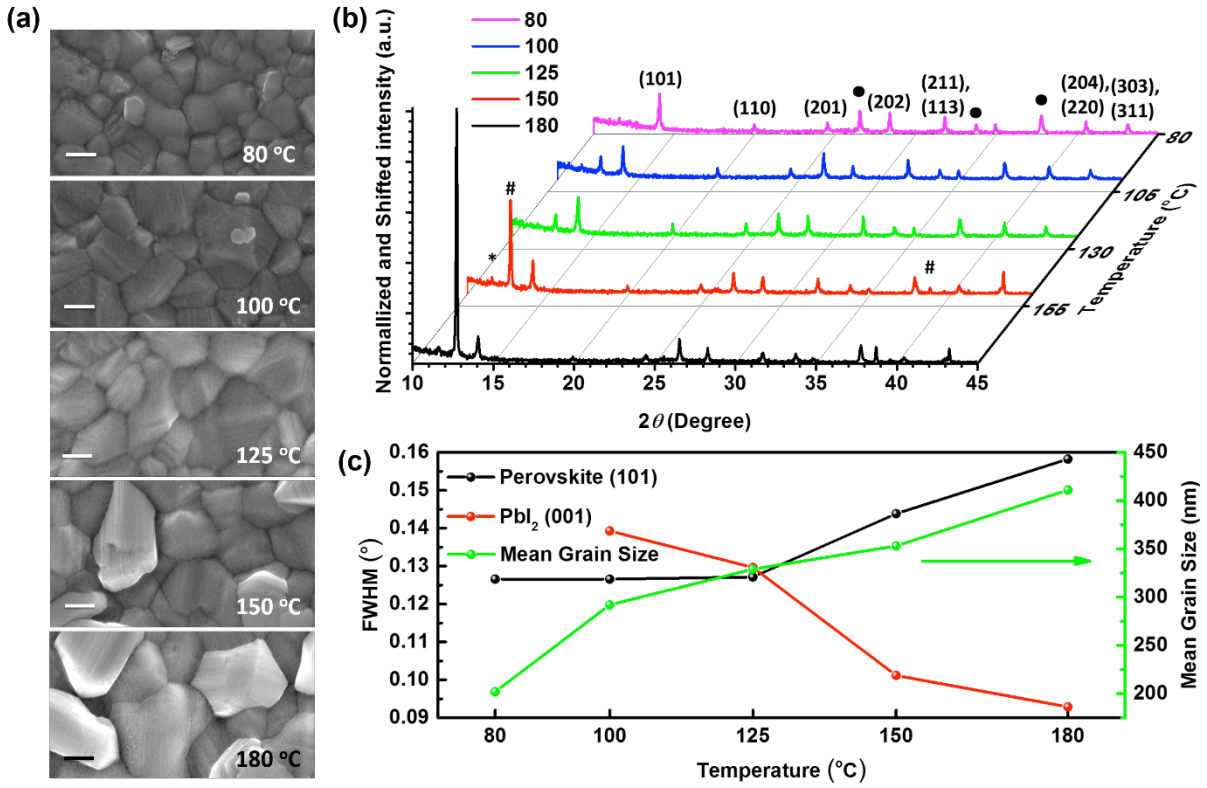

Figure 1. Morphology of compositive perovskite films annealed at 80°C, 100°C, 125°C, 150°C and 180°C. (a). Top-view SEM images, Scale bars, 200 nm; (b) Indexed X-ray diffraction patterns of the deposited films on meso-TiO_2/c-TiO_2/FTO glass substrates after annealing at various temperatures for 90 min. *, # and ● denote the identified diffraction peaks corresponding to the non-perovskite polymorphs of $FAPbI_3$, PbI_2 and FTO, respectively. (c). Temperature-dependent X-ray diffraction (101) peak of perovskite and (001) peak of PbI_2 full width at half maximum (FWHM) (left Y axis) and average grain size of the films (right Y axis).

Figure 1b shows the X-ray diffraction (XRD) patterns of the prepared composite perovskite ($(FAPbI_3)_{0.85}(MAPbBr_3)_{0.15}$) films on meso-$TiO_2$/c-$TiO_2$/FTO glass substrates, after annealing at different temperature for 120 min. Characteristic diffraction peaks, belonging to the trigonal perovskite phase (P3m1), can be observed with all the patterns.[23] Except for the film annealed at 80°C, a peak at around 12.68 corresponding to the PbI_2 (001) reflection is observed for the rest of the samples, indicating the formation of PbI_2 phases after releasing the organic species during annealing.

Traces of yellow FAPbI3 polymorph is also observed. In Figure 1c, the full width at half maximum (FWHM) of the (001) reflection of PbI_2 is found to decrease with increasing annealing temperature, which is indicative of the increase in the X-ray crystallite size. On the other hand, the FWHM of (101) reflections of the perovskite phase showed almost no change below 125^{o}C and starts to increase quickly above 125^{o}C. This is due to the increased conversion of perovskite to PbI_2 and therefore a decrease in perovskite crystallite size.

We evaluated the influence of the annealing temperature of the composite perovskite film on photovoltaic device performance by controlled grain growth and self-generated PbI_2 phases. All the devices have a structure of FTO/c-TiO_2/meso-TiO_2/compositive perovskite/Spiro-OMeTAD/Au and current-voltage characteristics are measured under simulated air mass (AM) 1.5 irradiance of 100 mW/cm^2 with a mask area of 0.16 cm^2 as previously reported[19] (Fig. 2a-d), It is interesting to note that the V_{OC} keeps increasing despite the enlargement of PbI_2 crystallite size until 150 ^{o}C with an average maximum of 1.11 V. We have addressed the reasons of the observed Voc change in detail already in our previous study [19]. This dealt also with the effect of excess PbI_2 on the optoelectronic and specifically the photovoltaic metrics of $(FAPbI_3)_{0.85}(MAPbBr_3)_{0.15}$ based perovskite films. In contrast to the preset study this excess was produced by adding a stoichiometric excess of PbI_2 to the perovskite solution instead of releasing MAI from the perovskite lattice lattice by heat treatment. The variation of the Voc with PbI_2 content correlated with non-radiative charge carrier recombination whose rate was measured by time resolved photoluminescence. We have found a similar correlation of PL-lifetimes with the Voc variations induced by thermal loss of MAI from the lattice indicating that both methods produce similar effects. (Figure S4) Moreover as the thermally induced loss of

MAI produces excess PbI_2 mostly on the surface of the perovskite grains we can infer from the present study that the retardation of nonradiative recombination by PbI_2 is most likely due to a surface passivation of the perovskite by PbI_2.

J_{SC} and FF start to deteriorate upon annealing at temperatures of >100 ^{o}C. Therefore, the best PCE was obtained at 100 ^{o}C mainly due to the highest average J_{SC} (23.1 mA/cm^2), at which temperature the mean grain size is around 329 nm. The dependence of J_{SC} and FF on the PbI_2 content is different from the behavior observed when extra PbI_2 is added to the precursor solution, where no significant change is observed over a large range of PbI_2 excess contents.[19] The PbI_2 generated in-situ at high temperature above 100 ^{o}C reduces J_{SC} and FF very quickly. When the film is annealed at 180 ^{o}C, prominent PbI_2 phase is observed as indicated by the slight color bleaching and the strong XRD diffraction peak of PbI_2. Nevertheless, the mean V_{OC} is still as high as 1.07 V, while the J_{SC} and FF decline substantially to 19.5 mA/cm^2 and 0.55, respectively. Therefore, due to the trade-off effect among V_{OC}, J_{SC} and FF, the highest performance is obtained from the compositive perovskite film annealed at 100 ^{o}C, which will be used as the optimal temperature for further morphology engineering.

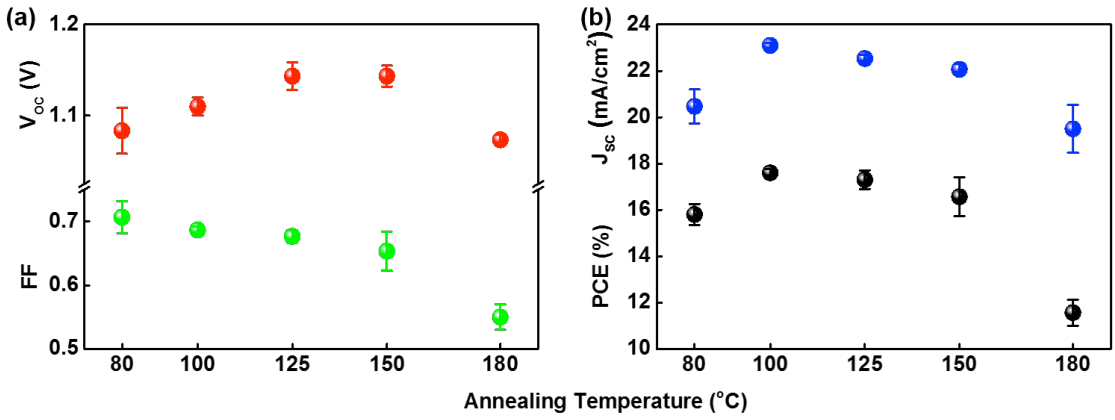

Figure 2. Influence of annealing temperature on photovoltaic parameters of the fabricated solar cells. J_{SC} (A), V_{OC} (B),

FF (C), and PCE (D) versus temperature, measured under AM 1.5 G illumination (100 mW cm^{-2}). Error bars represent minimum and maximum values. Detailed statistics are shown in supplementary information, Table S1.

Besides annealing temperature, the precursor concentrations also have significant effects on the quality and morphology of the spin casted films.[24–28] To further optimize the composite perovskite film and find condition for reproducible high performance devices, a series of six precursor solutions with different concentration are used to deposit the perovskite film with the same optimized annealing temperature and hence the same degree of PbI_2 generation. We employed SEM to investigate how the morphology of the perovskite layer evolved with concentration. Figure 3a compares cross-sectional and top-view SEM images of the perovskite layer as a function of the precursor concentration. As expected, the thickness of the film is proportional to the solution concentration, from 100 nm-thick film out of 0.88 M solution to 1035 nm-thick film out of 2 M. (Figure 3d). From Figure 3a, the morphology of perovskite behaves quite differently depending on the solution concentration range. The statistics of grain size derived from their corresponding SEM images (Figure S2) are shown in Figure 3d. The mean grain size of the films increases slowly from 128.19 nm to 292 nm when the concentration of solution increase to 1.52 M. After that the grain size is almost constant until 2 M. Based on these measurements, we calculated the average grain size/thickness aspect ratio of the films, the value of which is decreasing along with the increase of thickness. (Figure 3d) From 1.35 M to 1.7 M, the grain size and thickness grow with the same rate. So the aspect ratio almost stabilized between 0.5 and 0.6.

Figure 3b displays XRD profiles of FTO/c-TiO_2/meso-TiO_2/perovskite structures prepared with different precursor concentration. Due to the same annealing temperature of 100 ^oC, PbI_2 (001) is

observed for all the samples. It should be emphasized that the sample from a concentration of 1.35 M is made with the optimized condition from previous step, so the XRD pattern looks the same. When the concentration is as low as 0.88 M, the film is so thin that only the signals of FTO are clearly shown. From 1.06 M, we have all the diffraction peaks of perovskite and PbI_2. To analyze the crystallite size, we fitted the diffraction peaks of PbI_2 (001) and perovskite (101) reflections and calculated their FWHM. (Figure 3c) At the same annealing temperature, the generated PbI_2 phase in different films have similar crystallite size with little decrease between 1.06 M and 1.52 M. The crystallite size of perovskite, however, varies strongly with the concentration. At the concentration of 1.35 M, the FWHM of (101) reflections reach the minimum indicating the largest crystallite size. After that the FWHM increase with increased perovskite concentration, a phenomenon reported previously.[29]

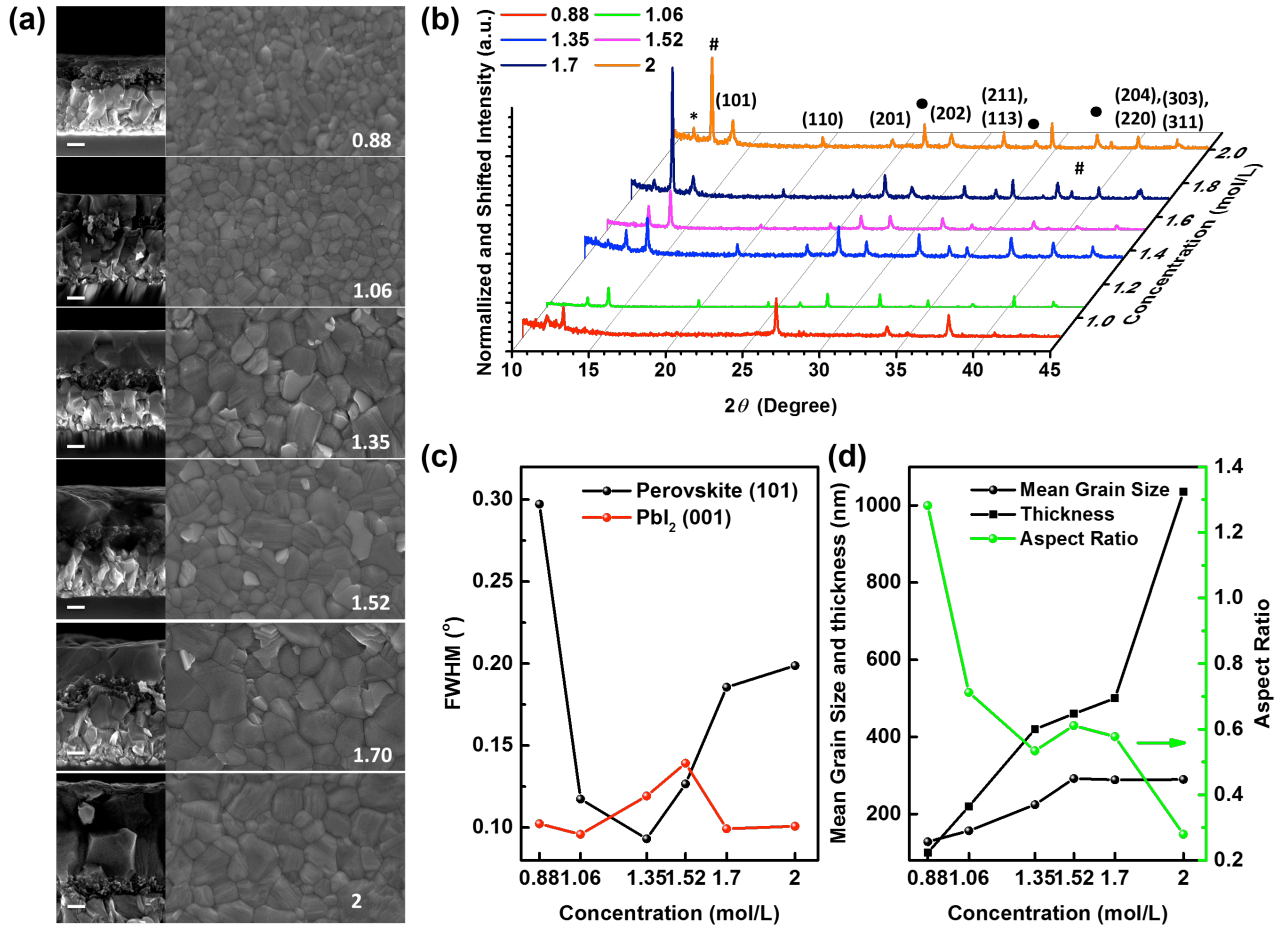

Figure 3. Morphology of compositive perovskite films made with different concentrations of perovskite precursor (0.88, 1.06, 1.35, 1.52, 1.7 and 2 mmol/ml). (a). Cross-sectional and top-view SEM images, Scale bars, 200 nm; (b). Indexed X-ray diffraction patterns of the deposited films on meso-TiO_2/c-TiO_2/FTO glass substrates annealed at 100 ^oC for 90 min. *, # and ● denote the identified diffraction peaks corresponding to the non-perovskite polymorphs of $FAPbI_3$, PbI_2 and FTO, respectively. (c). Concentration-dependent X-ray diffraction (101) peak of perovskite and (001) peak of PbI_2 full width at half maximum (FWHM). (d). Average grain size and thickness of perovskite layer (mesoporous + capping layer) (left Y axis) and average grain size/thickness aspect ratio (right Y axis).

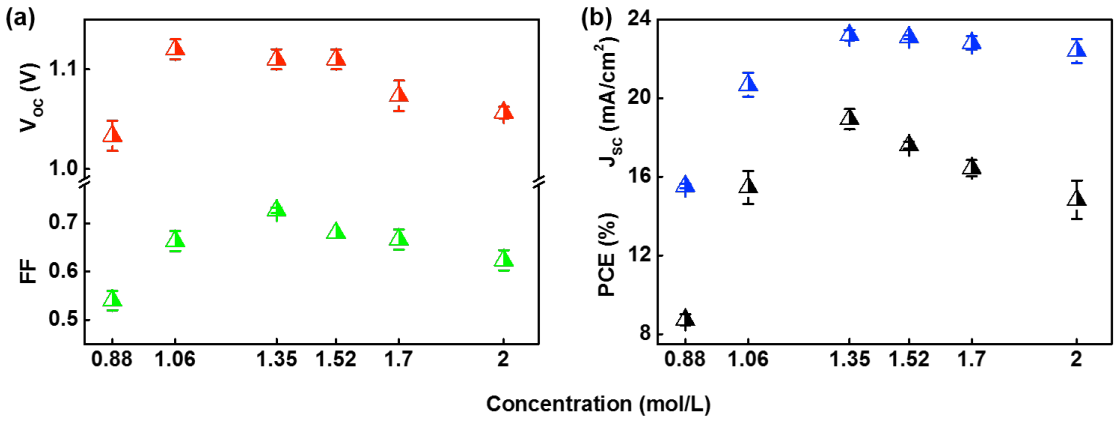

Figure 4. Influence of concentration on photovoltaic parameters of the fabricated solar cells. J_{SC} (A), V_{OC} (B), FF (C), and PCE (D) versus temperature, measured under AM 1.5 G illumination (100 mW cm^{-2}). Error bars represents minimum and maximum values. Detailed statistics are shown in supplementary information, Table S2.

Average photovoltaic parameters with standard deviation are listed in Table S2 and the dependence of the photovoltaic parameters on perovskite concentration is plotted in Figure 4. In Figure 4a, the devices made with concentration of 1.06 M, 1.35 M and 1.52 M show the highest average V_{OC} above 1.1 V. It is worth noting that these three concentrations give the largest X-ray crystallite size. At the same time, the average J_{SC} increases gradually with the perovskite concentration to a maximum of 23.2 mA/cm^2 at a concentration of 1.35 M. After that the J_{SC} stay above 22 mA/cm^2 until the concentration of 1.7 M giving a film thickness over 400 nm. This is remarkable and reasonable because of the extremely high charge carrier diffusion length that can overcome the increased thickness.[30] The FF is more sensitive to the concentration with the highest average value of 0.73 at 1.35 M. Consequently, after the optimization of precursor concentration, combining all the other optimized factors, the highest average PCE of 18.93% is attained with 1.35 M precursor solution along with the largest perovskite crystallite size. The small standard deviation indicates good reproducibility of this optimized condition. More importantly, one of the optimized devices was sent

to an accredited photovoltaic calibration laboratory for certification, confirmed a power conversion efficiency of 19.08 % measured under standard AM1.5G reporting conditions. Detailed photovoltaics data for this device can be found in Supporting Information Figure S3.

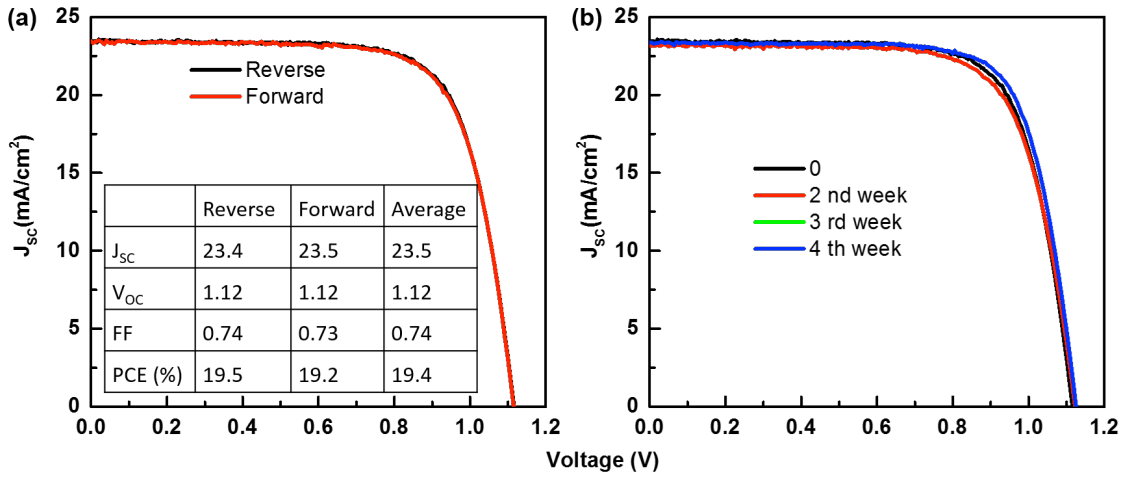

	Reverse	Forward	Average
J_{SC}	23.4	23.5	23.5
V_{OC}	1.12	1.12	1.12
FF	0.74	0.73	0.74
PCE (%)	19.5	19.2	19.4

Figure 5. Device performance of a fully optimized perovskite solar cell. (annealing temperature 100^{o}C and precursor concentration of 1.35 mol/L). (a). J-V curve obtained by reverse scan (1.17→0 V, step 0.005 V, delay time 0 ms) and forward scan (0 V→1.17V, step 0.005 V, delay time 0 ms) for the champion device under one sun conditions (100 mWcm-2, AM 1.5G). (b). Stability test of the sealed devices stored in the dry and dark condition.

The best performances based on this optimized condition is presented in Fig. 5a with different scan directions (reverse and forward). In the reverse scan direction, a 19.5 % PCE was achieved, yielding a J_{SC} of 23.4 mA cm^{-2}, V_{OC} of 1.12 V, and FF of 0.74. Negligible J–V hysteresis was observed in this type of devices as the PCE obtained from the forward scan (19.2%) was almost the same as that from reverse scan which indicates the successful morphology control and is in agreement with previous studies from our laboratories[19] and others.[4] These results, add more suspense to the origin of hysteresis[31] and preclude the necessity of n-type PCBM to eliminate the hysteresis effect.[32] Targeting commercialization of perovskite solar cells, we treat the stability as seriously as the photovoltaic

efficiency.[33] We test the stability of the sealed devices stored in dry and dark conditions. As shown in Fig. 5b, the four J-V curves measured within one month (an interval of one week) almost overlapped with each other. (Table S3) This stability condition ruled out the degradation mechanism of oxygen/water uptaking by amines and highlighted the morphology stability of the whole device. The excellent stability ensure that the devices fabricated under this condition can be sent to an independent laboratory for certification.

Conclusions

In conclusion, we have fabricated highly efficient and J-V hysteresis-free perovskite solar cells with reasonable stability based on a composite perovskite. The goal is realized through a two-fold morphology engineering. The first step is optimization of annealing temperature to control the self-generation of PbI_2. The concentration of precursor solution is controlled to obtain the crystallite size and film aspect ratio. Combining the benefit effect of PbI_2 phase and large perovskite crystallite, the composite perovskite spin-casted from a 1.35 M precursor solution showed the highest PCE of 19.5 % after annealing at 100 °C for 90 min. This work is on par with the very recent reports on record efficiency perovskite solar cells and addresses the intricacies of device engineering, grain growth, composition and microstructure. The study presented here is believed to benefit the whole perovskite photovoltaic community to fabricate reproducible high PCE polycrystalline thin film solar cells.

Experimental Section

Solar cell preparation

The fluorine-doped tin oxide coated glass (NSG.) was sequentially cleaned using detergent, acetone, and Ethanol. A 20-30 nm TiO_2 blocking layer was deposited on the cleaned FTO by spray pyrolysis using O_2 as the carrying gas at 450°C from a precursor solution of 0.6 ml titanium diisopropoxide and 0.4 ml bis(acetylacetonate) in 7 ml anhydrous Isopropanol. A 200 nm mesoporous TiO_2 was coated on the substrate by spin-coating with a speed of 4500 rpm for 15 s with a ramp of 2000 rpm s^{-1}, from a diluted 30 nm particle paste (Dyesol) in ethanol, the weight ratio of TiO_2 (Dyesol paste) and ethanol is 1:5.5. After spin coating, the substrate was immediately dried on a hotplate at 80°C, and then the substrates were sintered at 500°C for 20 min. The perovskite film was deposited by spin-coating onto the TiO_2 substrate. The $FA_{1-x}MA_xPb(I_{1-y}Br_y)$ precursor solution was prepared in glovebox from PbI_2 and $PbBr_2$ in the mixed solvent of DMF and DMSO, the concentration of the Pb^{2+} was varied as descibed in the main text. The volume ratio of DMF and DMSO is 4:1. The molar ratio of PbI_2 (TCI, purity 98%)/$PbBr_2$(Alfa. Aesa, purity, 99.999%) was fixed to 0.85:0.15, and the molar ratio of MABr/$PbBr_2$ was fixed to 1:1. The spin coating procedure was done in an argon flowing glovebox, first 2000 rpm for 10 s with a ramp of 200 rpm s^{-1}, second 6000 rpm for 30 s with a ramp of 2000 rpm s^{-1}. 110 ul chlorobenzene was dropped on the spinning substrate during the second spincoating step 20 s before the end of the procedure. The substrate was then heated for 90 min on a hotplate. The heating temperature was varied as described in the main text. After cooling down to room temperature, Spiro-OMeTAD (Merck) was subsequently deposited on the top of the perovskite layer by spin coating at 3000 rpm for 20 s. The Spiro-OMeTAD solutions were prepared dissolving the spiro-OMeTAD in chlorobenzene at a concentration of 60 mM, with the addition of 30 mM bis(trifluoromethanesulfonyl)imide from a stock solution in acetonitrile), and 200 mM of

tert-butylpyridine. Finally, FK209(Tris(2-(1H-pyrazol-1-yl)-4-tert-butylpyridine)- cobalt(III) Tris(bis(trifluoromethylsulfonyl)imide)) (Dyenamo A B.) was added to the spiro-OMeTAD solution, from a stock solution in acetonitrile, the molar ratio of FK209 and Spiro-OMeTAD is 0.03. Finally, 80 nm of gold was deposited by thermal evaporation using a shadow mask to pattern the electrodes.

Acknowledgment

We thank Dr. Peng Gao for helping with the SEM/XRD data analysis and editing the manuscript. We thank financial support from the Swiss National Science Foundation (SNSF), the SNSF NRP 70 "Energy Turnaround", CCEM-CH in the 9th call proposal 906: CONNECT PV, as well as from SNF-NanoTera (SYNERGY) and Swiss Federal Office of Energy (SYNERGY), the European Union's Horizon 2020 research and innovation program under the grant agreement No 687008 (GOTSolar) is gratefully acknowledged.

The information and views set out in this article are those of the author(s) and do not necessarily reflect the official opinion of the European Union. Neither the European Union institutions and bodies nor any person acting on their behalf may be held responsible for the use that which may be made of the information contained herein.

References

(1) http://www.nrel.gov/ncpv/images/efficiency_chart.jpg. National Renewable Energy Laboratory Best Research-Cell Efficiencies http://www.nrel.gov/ncpv/images/efficiency_chart.jpg.

(2) Gao, P.; Grätzel, M.; Nazeeruddin, M. K. *Energy Environ. Sci.* **2014**, *7*, 2448.

(3) Pellet, N.; Gao, P.; Gregori, G.; Yang, T.-Y.; Nazeeruddin, M. K.; Maier, J.; Grätzel, M. *Angew. Chemie Int. Ed.* **2014**, *53*, 3151–3157.

(4) Jeon, N. J.; Noh, J. H.; Yang, W. S.; Kim, Y. C.; Ryu, S.; Seo, J.; Seok, S. Il. *Nature* **2015**, *517*, 476–480.

(5) Yang, W. S.; Noh, J. H.; Jeon, N. J.; Kim, Y. C.; Ryu, S.; Seo, J.; Seok, S. Il. *Science (80-.).* **2015**, *348*, 1234–1237.

(6) Ahn, N.; Son, D.-Y.; Jang, I.-H.; Kang, S. M.; Choi, M.; Park, N.-G. *J. Am. Chem. Soc.* **2015**, *137*, 8696–8699.

(7) Zhou, H.; Chen, Q.; Li, G.; Luo, S.; Song, T. -b.; Duan, H.-S.; Hong, Z.; You, J.; Liu, Y.; Yang, Y. *Science (80-.).* **2014**, *345*, 542–546.

(8) Jeon, N. J.; Noh, J. H.; Kim, Y. C.; Yang, W. S.; Ryu, S.; Seok, S. Il. *Nat. Mater.* **2014**, *13*, 897–903.

(9) Xiao, M.; Huang, F.; Huang, W.; Dkhissi, Y.; Zhu, Y.; Etheridge, J.; Gray-Weale, A.; Bach, U.; Cheng, Y.-B.; Spiccia, L. *Angew. Chemie Int. Ed.* **2014**, *53*, 9898–9903.

(10) Huang, F.; Dkhissi, Y.; Huang, W.; Xiao, M.; Benesperi, I.; Rubanov, S.; Zhu, Y.; Lin, X.; Jiang, L.; Zhou, Y.; Gray-Weale, A.; Etheridge, J.; McNeill, C. R.; Caruso, R. a.; Bach, U.;

Spiccia, L.; Cheng, Y.-B. *Nano Energy* **2014**, *10*, 10–18.

(11) Hu, Q.; Wu, J.; Jiang, C.; Liu, T.; Que, X.; Zhu, R.; Gong, Q. *ACS Nano* **2014**, *8*, 10161–10167.

(12) Wang, K.-C.; Jeng, J.-Y.; Shen, P.-S.; Chang, Y.-C.; Diau, E. W.-G.; Tsai, C.-H.; Chao, T.-Y.; Hsu, H.-C.; Lin, P.-Y.; Chen, P.; Guo, T.-F.; Wen, T.-C. *Sci. Rep.* **2014**, *4*, 4756.

(13) Etgar, L.; Gao, P.; Xue, Z.; Peng, Q.; Chandiran, A. K.; Liu, B.; Nazeeruddin, M. K.; Grätzel, M. *J. Am. Chem. Soc.* **2012**, *134*, 17396–17399.

(14) Liu, D.; Yang, J.; Kelly, T. L. *J. Am. Chem. Soc.* **2014**, *136*, 17116–17122.

(15) Liu, M.; Johnston, M. B.; Snaith, H. J. *Nature* **2013**, *501*, 395–398.

(16) Dualeh, A.; Tétreault, N.; Moehl, T.; Gao, P.; Nazeeruddin, M. K.; Grätzel, M. *Adv. Funct. Mater.* **2014**, *24*, 3250–3258.

(17) Bi, D.; El-Zohry, A. M.; Hagfeldt, A.; Boschloo, G. *ACS Photonics* **2015**, *2*, 589–594.

(18) Im, J.-H.; Jang, I.-H.; Pellet, N.; Grätzel, M.; Park, N.-G. *Nat. Nanotechnol.* **2014**, *9*, 927–932.

(19) Bi, D.; Tress, W.; Dar, M. I.; Gao, P.; Luo, J.; Renevier, C.; Schenk, K.; Abate, A.; Giordano, F.; Correa Baena, J.-P.; Decoppet, J.-D.; Zakeeruddin, S. M.; Nazeeruddin, M. K.; Gra tzel, M.; Hagfeldt, A. *Sci. Adv.* **2016**, *2*, e1501170–e1501170.

(20) Chen, Q.; Zhou, H.; Song, T.-B.; Luo, S.; Hong, Z.; Duan, H.-S.; Dou, L.; Liu, Y.; Yang, Y. *Nano Lett.* **2014**, *14*, 4158–4163.

(21) Thompson, C. V. *Annu. Rev. Mater. Sci.* **2000**, *30*, 159–190.

(22) Pritula, I.; Sangwal, K. In *Handbook of Crystal Growth*; Elsevier, 2015; pp. 1185–1227.

(23) Koh, T. M.; Fu, K.; Fang, Y.; Chen, S.; Sum, T. C.; Mathews, N.; Mhaisalkar, S. G.; Boix, P. P.; Baikie, T. *J. Phys. Chem. C* **2014**, *118*, 16458–16462.

(24) Hsu, H.-L.; Chen, C.; Chang, J.-Y.; Yu, Y.-Y.; Shen, Y.-K. *Nanoscale* **2014**, *6*, 10281–10288.

(25) Chen, C.-C.; Hong, Z.; Li, G.; Chen, Q.; Zhou, H.; Yang, Y. *J. Photonics Energy* **2015**, *5*, 057405.

(26) Conings, B.; Baeten, L.; De Dobbelaere, C.; D'Haen, J.; Manca, J.; Boyen, H.-G. *Adv. Mater.* **2014**, *26*, 2041–2046.

(27) Yu, Y.-Y.; Chiang, R.-S.; Hsu, H.-L.; Yang, C.-C.; Chen, C.-P. *Nanoscale* **2014**, *6*, 11403–11410.

(28) Eperon, G. E.; Burlakov, V. M.; Docampo, P.; Goriely, A.; Snaith, H. J. *Adv. Funct. Mater.* **2014**, *24*, 151–157.

(29) Seol, D.-J.; Lee, J.-W.; Park, N.-G. *ChemSusChem* **2015**, *8*, 2414–2419.

(30) Dong, Q.; Fang, Y.; Shao, Y.; Mulligan, P.; Qiu, J.; Cao, L.; Huang, J. *Science (80-.).* **2015**, *347*, 967–970.

(31) Snaith, H. J.; Abate, A.; Ball, J. M.; Eperon, G. E.; Leijtens, T.; Noel, N. K.; Stranks, S. D.; Wang, J. T.-W.; Wojciechowski, K.; Zhang, W. *J. Phys. Chem. Lett.* **2014**, *5*, 1511–1515.

(32) Shao, Y.; Xiao, Z.; Bi, C.; Yuan, Y.; Huang, J. *Nat. Commun.* **2014**, *5*, 5784.

(33) Bi, D.; Gao, P.; Scopelliti, R.; Oveisi, E.; Luo, J.; Grätzel, M.; Hagfeldt, A.; Nazeeruddin, M. K. *Adv. Mater.* **2016**, 10.1002/adma.201505255.

Supporting Information

Characterization

Current–voltage characteristics were recorded by applying an external potential bias to the cell while recording the generated photocurrent with a digital source meter (Keithley Model 2400). The light source was a 450-W xenon lamp (Oriel) equipped with a Schott K113 Tempax sunlight filter (Praezisions Glas & Optik GmbH) to match the emission spectrum of the lamp to the AM1.5G standard. Before each measurement, the exact light intensity was determined using a calibrated Si reference diode equipped with an infrared cut-off filter (KG-3, Schott).

X-ray diffraction (XRD) spectra were recorded on an X'Pert MPD PRO (PANalytical) equipped with a ceramic tube providing Ni-filtered (CuK✔ ✁ = 1.54060 Å) radiation and a RTMS X'Celerator (PANalytical). The measurements were done in BRAGG-BRENTANO geometry from 2 ✂= 8 to 88°. The samples were mounted without further modification and the automatic divergence slit (10 mm) and beam mask (10 mm) were adjusted to the dimension of the films. A step size of 0.008° was chosen for an acquisition time of 270.57 s deg^{-1}. A baseline correction was applied to all X-Ray powder diffractograms to compensate for the broad feature arising from the FTO glass and anatase substrate.

Scanning electron microscope (SEM) images were recorded using a high-resolution scanning electron microscope (ZEISS Merlin). Statistics of grain size distribution were conducted by transfer SEM images with size of 2.5 ✄ m × 2.75 ✄ m to a high contrast color mode by software of "wyddion". The SEM images with size bars on each grain were shown in Fig. S1 and Fig S2. These size bars

were manually marked for each grain, and the grain size data was collected by software "wyddion". The grains have irregular shapes. In order to get accurate size distribution, all the size bars were aligned in the same direction, and all grains in the images were included in the statistics without selection following the method reported before.[1] Fig. S1 and Fig. S2 also show the histograms of distribution statistics of grain size.

Tables S1. Photovoltaic parameters of the devices for optimizing annealing temperature.

Temperature	Voc (V)	Average (V)/S.D.	Jsc (mA/cm^2)	Average (mA/cm^2) /S.D.	FF	Average/S.D.	PCE (%)	Average (%)/S.D.
80	1.06	1.08333/ 0.02517	21.3	20.46667/ 0.73711	0.71	0.70667/ 0.02517	16.2	15.8/ 0.45826
	1.08		19.9		0.73		15.9	
	1.11		20.2		0.68		15.3	
100	1.1	1.11/ 0.01	23.2	23.1/ 0.1	0.682	0.6864/ 0.00601	17.4	17.6/ 0.17321
	1.12		23.1		0.6841		17.7	

[1] Q. Dong, Y. Yuan, Y. Shao, Y. Fang, Q. Wang, J. Huang, Energy Environ. Sci. 2015, 8, 2464.

	1.11		23.0		0.6933		17.7	
125	1.13	1.14333/ 0.01528	22.4	22.53333/ 0.15275	0.6654	0.67/0.01	17.4	17.2/ 0.40415
	1.16		22.5		0.6798		17.1	
	1.14		22.7		0.657		17.1	
150	1.15	1.14333/ 0.01155	22.3	22.06667/ 0.25166	0.66	0.65333/0.03055	17	16.6/ 0.83865
	1.15		21.8		0.62		15.6	
	1.13		22.1		0.68		17.1	
180	1.07	1.07333/ 0.00577	20	19.5/ 1.04403	0.57	0.55/ 0.02	12.2	11.6/ 0.56862
	1.07		20.2		0.53		11.4	
	1.08		18.3		0.55		11.1	

Tables S2. Photovoltaic parameters of the devices for optimizing concentration.

Concentration	**Voc (V)**	**Average (V) /S.D.**	**Jsc (mA/cm^2)**	**Average (mA/cm^2) /S.D.**	**FF**	**Average/S.D.**	**PCE (%)**	**Average (%)/S.D.**
0.88	1.02	1.03333/ 0.01528	15.6	15.53333/ 0.11547	0.52	0.54/ 0.02	8.4	8.73333/0.28868
	1.05		15.6		0.54		8.9	
	1.03		15.4		0.56		8.9	
1.06	1.13	1.12/ 0.01	20	20.66667/ 0.61101	0.64	0.66333/ 0.02082	14.5	15.46667/0.8387
	1.12		21.2		0.67		16	

	1.11		20.8		0.68		15.9	
1.35	1.12	1.11/ 0.01	23.4	23.2/ 0.26458	0.74	0.73/ 0.00577	19.4	18.9/0.51316
	1.1		23.1		0.73		18.5	
	1.11		23		0.72		18.8	
1.52	1.1	1.11/ 0.01	23	23.1/ 0.1	0.682	0.6864/ 0.00601	17.4	17.6/0.17321
	1.12		23.1		0.6841		17.7	
	1.11		23.2		0.6933		17.7	
1.7	1.06	1.07333/ 0.01528	23	22.8/ 0.34641	0.65	0.66667/0.02082	16.3	16.43333/0.4163
	1.07		23		0.66		16.1	
	1.09		22.4		0.69		16.9	
2.0	1.06	1.05667/ 0.00577	22.7	22.4/ 0.60828	0.64	0.62333/0.02082	15.5	14.83333/0.9866
	1.06		21.7		0.6		13.7	
	1.05		22.8		0.63		15.3	

Tables S3. Stability test of one typical cell.

Time	**Voc (V)**	**Jsc (mA/cm^2)**	**FF**	**PCE (%)**
0	1.12	23.4	0.74	19.4
2nd week	1.12	23.2	0.72	19
3rd week	1.13	23.3	0.75	19.8
4th week	1.13	23.2	0.75	19.8

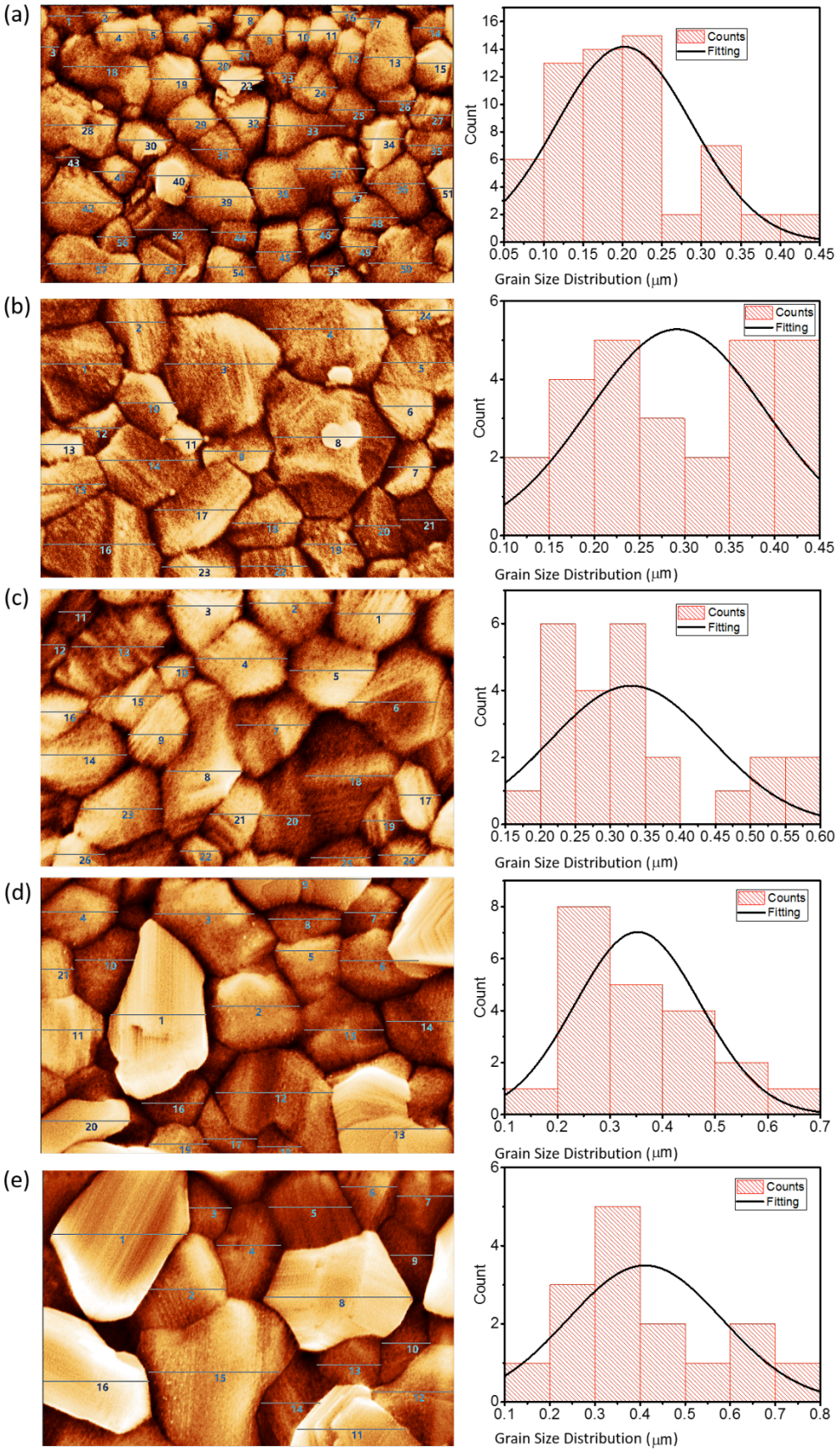
(a)
Counts
Fitting
Count
Grain Size Distribution (μm)
(b)
Counts
Fitting
Count
Grain Size Distribution (μm)
(c)
Counts
Fitting
Count
Grain Size Distribution (μm)
(d)
Counts
Fitting
Count
Grain Size Distribution (μm)
(e)
Counts
Fitting
Count
Grain Size Distribution (μm)

Figure S1. SEM images and grain size distribution histograms of compositive perovskite films annealed at 80^{o}C, 100^{o}C, 125^{o}C, 150^{o}C and 180^{o}C for the statistics of grain size with high contrast color mode. Image size was 2.5 ¦ m × 2.75 ¦ m.

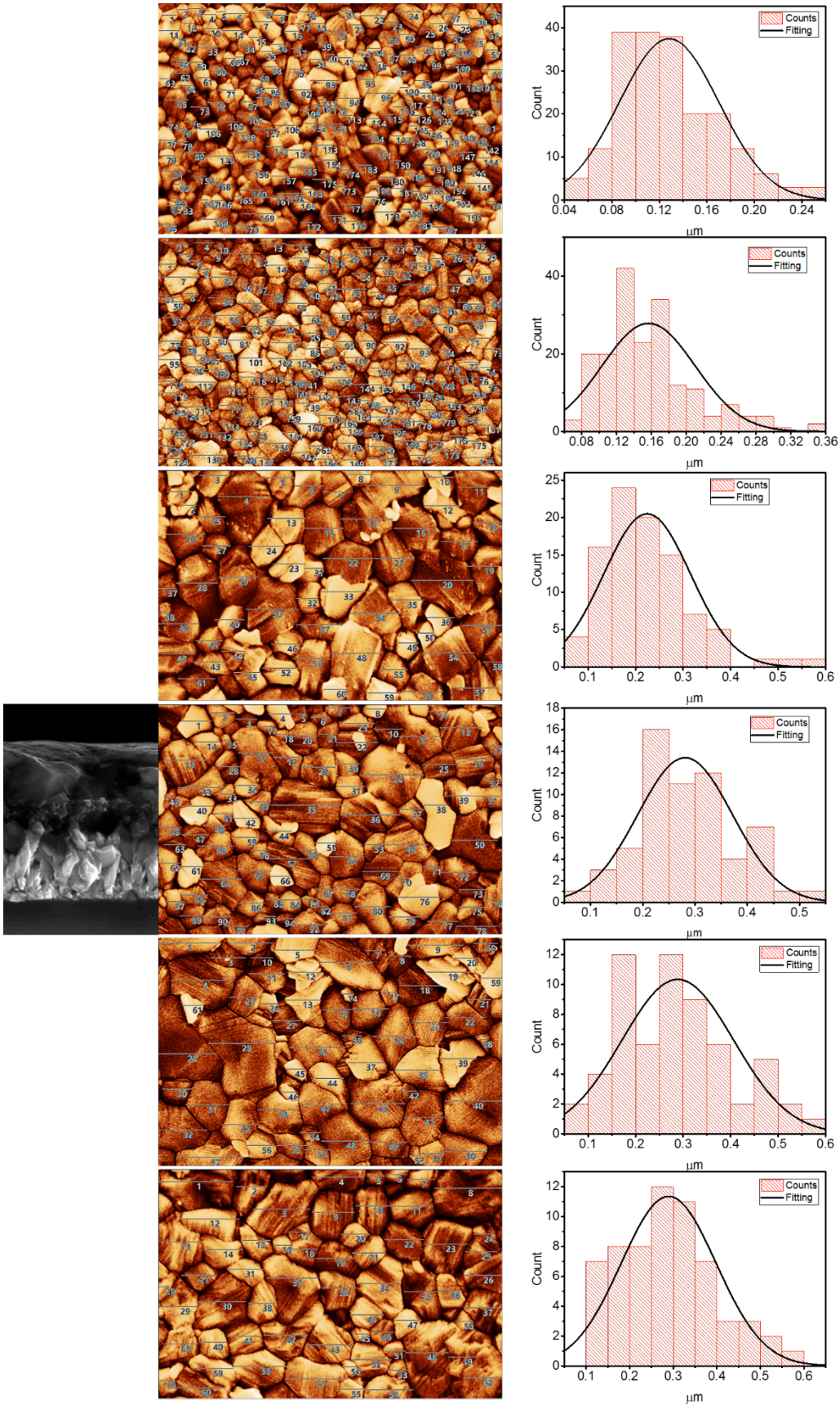

Figure S2. SEM images and grain size distribution histograms of compositive perovskite films made

with different concentrations of perovskite precursor (0.88, 1.06, 1.35, 1.52, 1.7 and 2 mol/l) for the statistics of grain size with high contrast color mode. Image size was 2.5 μm × 2.75 μm.

Newport	ACCREDITED Calibration Cert. # 2893.01	Technology and Application Center **PV Lab** Newport Calibration Cert. # 1171

DUT S/N: N6
Newport Calibration #: 1171
Manufacturer: Ecole Polytechnique Federale de Lausanne
Material: Perovskite
Temperature Sensor: None
Environmental conditions at the time of calibration: Temperature: 23 ± 1 °C; Humidity: 45 ± 2%

The above DUT has been tested using the following methods to meet the ISO 17025 Standard by the PV Lab at Newport Corporation. Quoted uncertainties are expanded using a coverage factor of $k = 2$ and expressed with an approximately 95% level of confidence. Measurement of total irradiance is traceable to the World Radiometric Reference (WRR) and all other measurements and uncertainties are traceable to either NIST or CNRC and the International System of Units (SI). The performance parameters reported in this certificate apply only at the time of the test, and do not imply future performance. NB: hysteresis was observed between forward and reverse scans.

Forward scan:

Efficency [%]	18.43	±	0.39	V_oc [V]	1.1295	±	0.0112	I_sc [A]	0.003667	±	0.000068
P_max [mW]	2.890	±	0.061	V_max [V]	0.8995	±	0.0089	I_max [A]	0.003213	±	0.000060
FF [%]	69.8	±	1.5	Area [cm^2]	0.1568	±	0.0003	M	0.978	±	0.004

Reverse scan:

Efficency [%]	19.08	±	0.40	V_oc [V]	1.1345	±	0.0112	I_sc [A]	0.003686	±	0.000069
P_max [mW]	2.991	±	0.063	V_max [V]	0.9161	±	0.0091	I_max [A]	0.003265	±	0.000061
FF [%]	71.5	±	1.5	Area [cm^2]	0.1568	±	0.0003	M	0.978	±	0.004

Methods:

I-V: ASTM E948-09 *Standard Test Method for Electrical Performance of Photovoltaic Cells Using Reference Cells Under Simulated Sunlight*

QE: ASTM E1021-06 *Standard Test Method for Spectral Responsivity Measurements of Photovoltaic Devices*

Standard Reporting Conditions:

Spectrum: AM1.5-G (ASTM G173-03/IEC 60904-3 ed. 2)
1000.0 W/m ^{2} at 25.0°C

Secondary Reference Cell:

Device S/N: PVM 284 KG5
Device Material: mono-Si
Window Material: KG5
Certification: National Renewable Energy Laboratory
A2LA accreditation certificate # 2236.01
ISO Tracking #: 1811
Certified short circuit current (I_{sc}) under standard reporting conditions (SRC): 33.803mA
Calibration due date: 11-Aug-15

Solar Simulator:

Spectrum: Newport Corporation filename *Sol3A_Spectroradiometer_Scan_0163.xls*
Total irradiance: 1000 W/m^2 based on I_{sc} of the above Secondary Reference Cell

Quantum Efficiency for DUT:

Newport Corporation filename *QE 1171.xls*
Spectral mismatch correction factor: M = 0.978 ± 0.004

DUT Calibration Procedures:

Newport Corporation document QE1021 V1_6
Newport Corporation document Area Measurement V1_4
Newport Corporation document PV948 V1_9

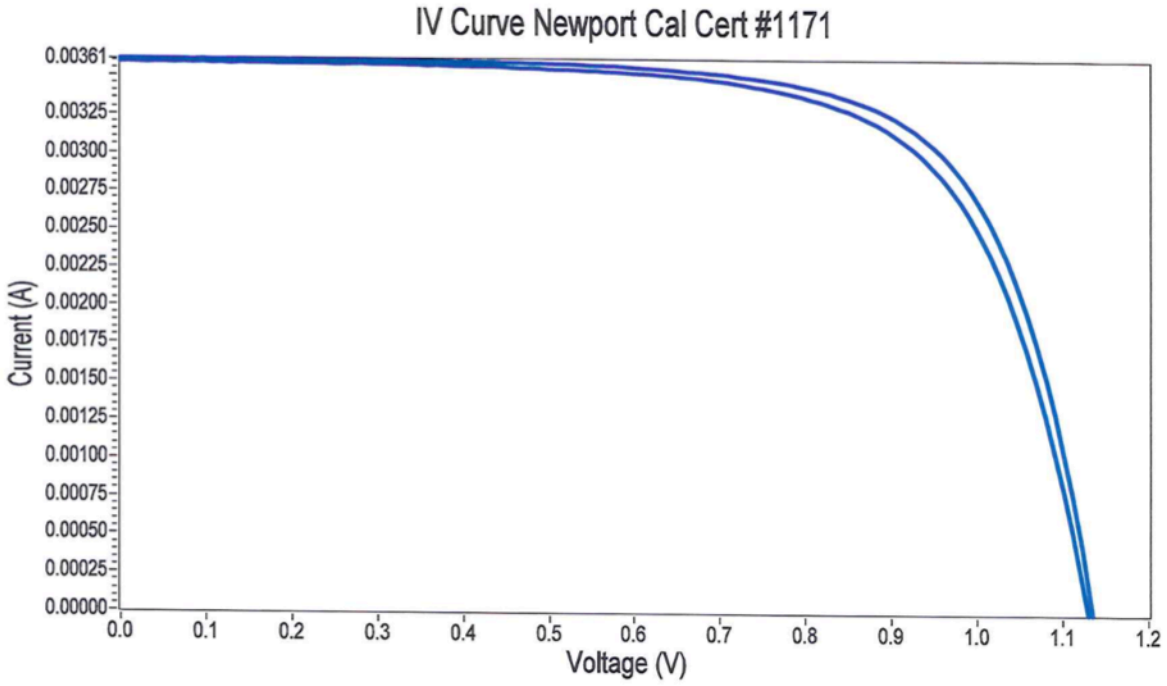
IV Curve Newport Cal Cert #1171
Current (A)
0.00361
0.00325
0.00300
0.00275
0.00250
0.00225
0.00200
0.00175
0.00150
0.00125
0.00100
0.00075
0.00050
0.00025
0.00000
0.0
0.1
0.2
0.3
0.4
0.5
0.6
0.7
0.8
0.9
1.0
1.1
1.2
Voltage (V)

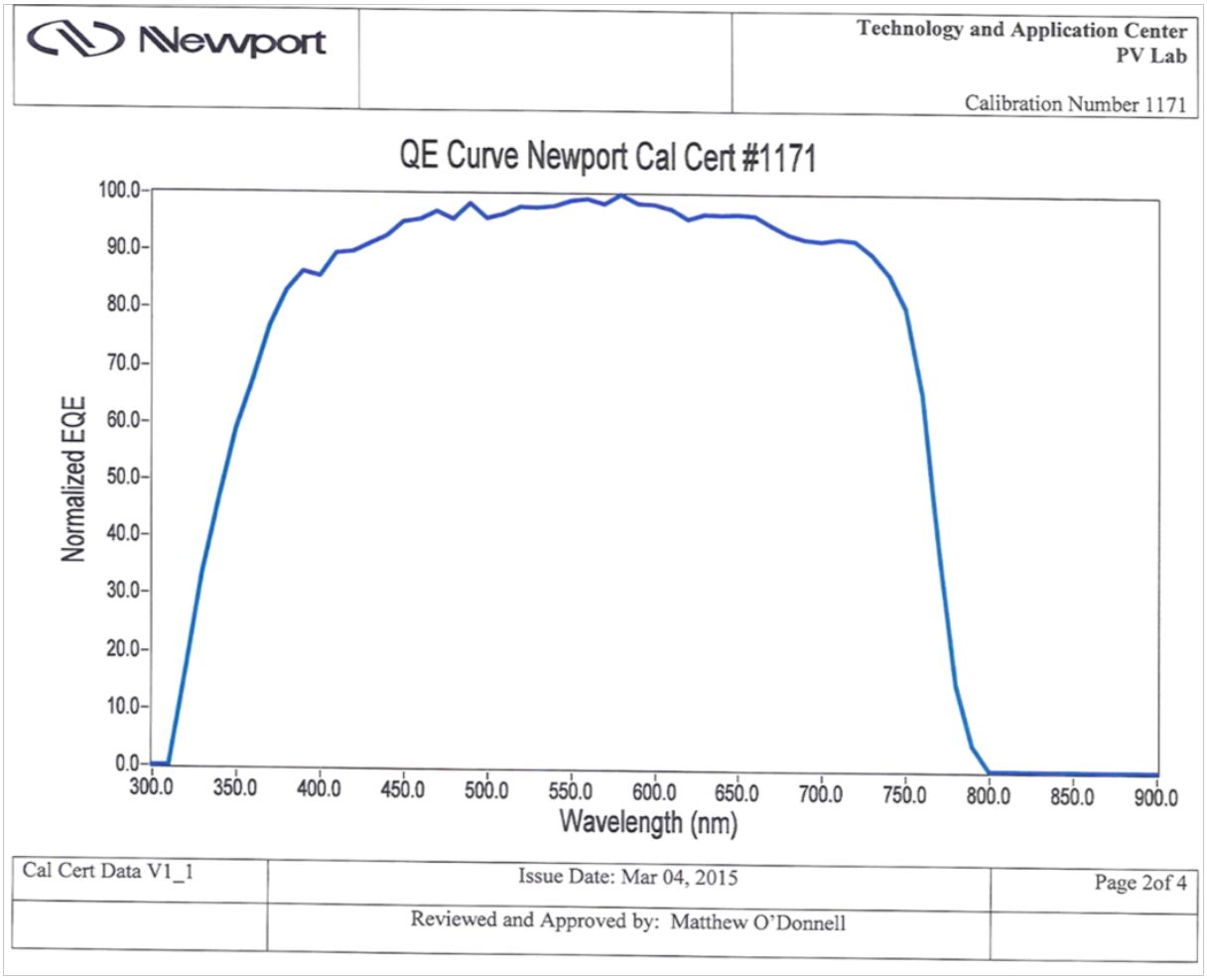

Figure S3. Independent certification from Newport Corporation confirming a PCE of 19.08 % (backward scan), 18.43% (forward scan) and a normalized EQE.

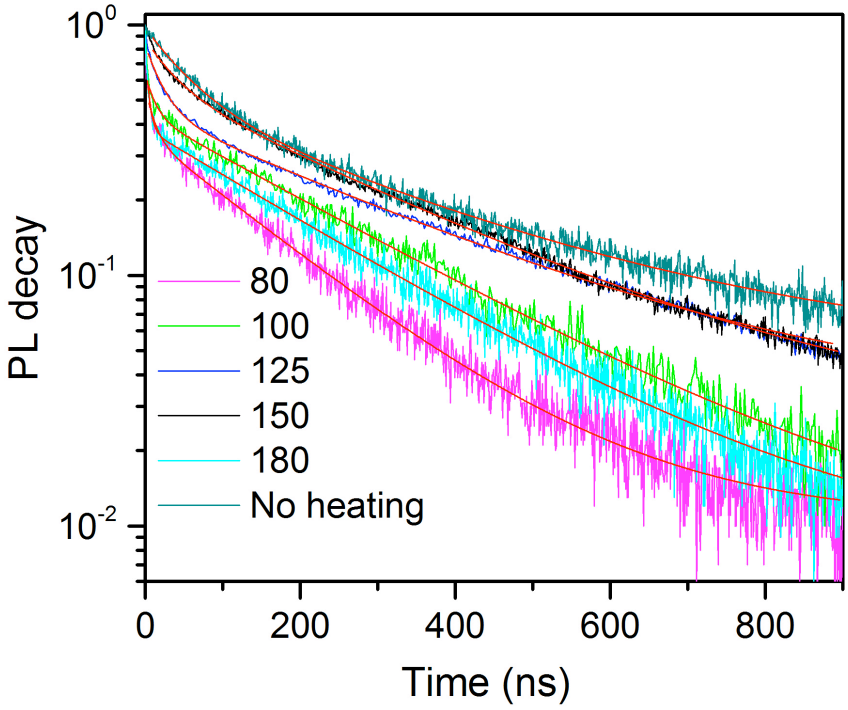

Figure S4. Transient phtoluminescence decay of the perovskite samples prepared at different temperature (℃).